



Decadal variability of eddy temperature fluxes in the Labrador Sea

Christopher Danek^{a,b,*}, Patrick Scholz^a, Gerrit Lohmann^{a,b}

^a Alfred Wegener Institute for Polar and Marine Research (AWI), Bremerhaven, Germany

^b MARUM-Center for Marine Environmental Sciences, Bremen, Germany



ARTICLE INFO

Keywords:

High-resolution
Labrador Sea
Mixed layer depth
Turbulence
Eddy kinetic energy

ABSTRACT

Small-scale eddies play an important role in preconditioning and restratifying the water column before and after mixing events, thereby affecting deep water formation variability. Results from a realistic eddy-resolving (~5 km local horizontal resolution) ocean model suggest that small-scale temperature fluxes due to turbulent potential to kinetic energy conversion are the main driver of mixed layer restratification during deep convection in the Labrador Sea interior and the West Greenland Current. This resupply of heat due to turbulent upward buoyancy fluxes exhibits a large interannual variability imposed by the atmospheric forcing. Eddy fluxes only become active in periods of strong buoyancy loss, while being quiescent otherwise. In a low-resolution (~20 km) control simulation the modeled turbulence is strongly reduced and the associated modeled and parameterized heat fluxes are too weak to increase stratification.

1. Introduction

Mesoscale eddies are ubiquitous in the world ocean (Chelton et al., 2011). On length scales of the local baroclinic Rossby radius of deformation these vortices yield mesoscale temperature and freshwater fluxes which modify sea water properties and thus change the ocean circulation, biogeochemical fluxes and mixed layer properties (Zhang et al., 2014; Fröb et al., 2016; Gaube et al., 2019).

The Labrador Sea (LS) is a region of frequent deep convection during winter and thereby an important place of deep water formation that contributes to overturning circulation and its variability (Rhein et al., 2017; Yeager et al., 2021). Here, eddies were observed to contribute to preconditioning before and restratification after deep convection as well as to enable the exchange of water masses between the interior and the boundary current (Marshall and Schott, 1999; Lilly et al., 2003; Straneo, 2006; Palter et al., 2008; de Jong et al., 2014; Rykova et al., 2015; Yashayaev and Loder, 2016; Zhang and Yan, 2018; Zou et al., 2021; Pacini and Pickart, 2022). However, the transfer of turbulent energy and associated mesoscale tracer fluxes remains unclear due to sparsity of available observations. Numerical model experiments suggest a complex interplay of barotropic and baroclinic instabilities as the source of eddy kinetic energy (EKE) and associated mesoscale tracer fluxes. During winter, Irminger Rings separate from the West Greenland Current (WGC), eventually providing buoyant waters for the weakly stratified LS interior. In addition, convective eddies in the vicinity of the deep convection patch as well as boundary current eddies work to

flatten steep isopycnals (Chanut et al., 2008; McGeehan and Maslowski, 2011; Kawasaki and Hasumi, 2014; Saenko et al., 2014; Zhang and Yan, 2014; Dukhovskoy et al., 2016; Rieck et al., 2019; Tagklis et al., 2020; Pennelly and Myers, 2022). In consequence, eddy contributions to the total heat flux were found to be, on average, as important as the mean circulation in the LS. However, no clear picture was provided, whether eddies act to reinforce or work against the mean circulation (Chanut et al., 2008; Kawasaki and Hasumi, 2014; Saenko et al., 2014; de Jong et al., 2016; Tagklis et al., 2020).

Due to the small local Rossby radius of deformation of <10 km and the complex geometry of the LS, numerical experiments with realistic high-resolution ocean models require high computational costs. Thus, the conducted model simulations in these previous studies usually cover a short period in time and focus on the mean state or the mean annual cycle. In this study we use the global ocean model FESOM (Danilov et al., 2004; Wang et al., 2014) with a locally mesoscale-resolving horizontal resolution of ~5 km and provide a coherent picture of turbulent kinetic energy and associated mesoscale temperature fluxes. We integrated the model for 310 years, to examine a decadal time-scale perspective of the complex LS mixed layer restratification dynamics. In addition, a low-resolution (~20 km local horizontal resolution) setup serves as control run to investigate the influence of the model resolution. This study hence aims to shed light on the temporal variability of mesoscale turbulence in the LS, as this was not provided earlier with a realistic high-resolution ocean model.

* Corresponding author at: Alfred Wegener Institute for Polar and Marine Research (AWI), Bremerhaven, Germany.
E-mail address: cdanek@awi.de (C. Danek).

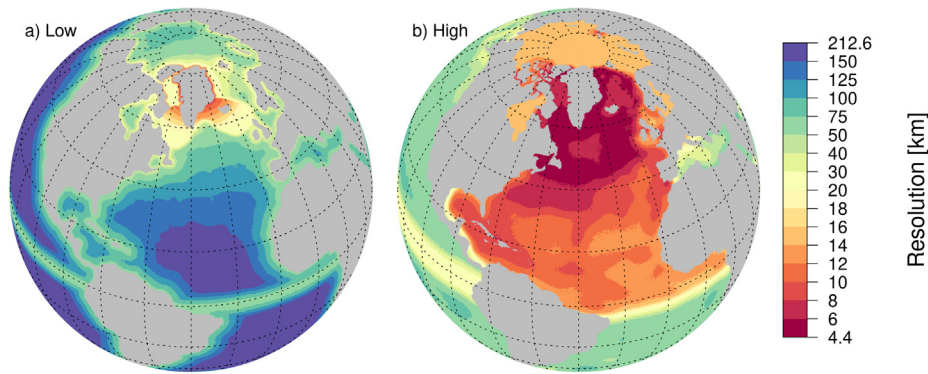


Fig. 1. Colors show horizontal resolution (in km) of the utilized low- (left) and high-resolution (right) FESOM setups. Orthographic projection realized with R packages *sf* (Pebesma, 2018) and *oce* (Kelley and Richards, 2022).

2. Methods

2.1. Ocean model FESOM

The global Finite Element Sea Ice–Ocean Model (FESOM) (Danilov et al., 2004; Wang et al., 2014) solves the governing equations for all variables of the ocean and sea ice on the vertices of tetrahedral elements of irregular size. A subgrid-scale (SGS) flux for parameterizing the eddy effects tracer mixing along isopycnals (Redi, 1982) and advection due to adiabatic stirring (Gent and McWilliams, 1990), formulated together as the Griffies skew flux (Griffies et al., 1998), was enabled and scaled with the local horizontal resolution and stratification of the flow. Diapycnal mixing is implemented via the k -profile parameterization (KPP) (Large et al., 1994). For salinity, a weak restoring was applied at the sea surface towards climatological values with a velocity of 50 m 300 days⁻¹. Density was calculated via the full equation of state (Jackett and McDougall, 1995), based on practical (and not absolute) salinity and in-situ or potential (and not conservative) temperature. Further model specifications can be found in Danek et al. (2019) and Wang et al. (2014). At the sea surface, FESOM was driven by the $\sim 1.8^\circ \times \sim 1.8^\circ$ atmospheric reanalysis dataset CORE-II (Large and Yeager, 2009) in an 6-h interval from 1948 to 2009 yielding a 62-year long simulation. This regular forcing data was bilinearly interpolated to the irregular FESOM grids. Following the CORE (Griffies et al., 2012) and OMIP (Griffies et al., 2016) protocols, we integrated FESOM for five complete forcing cycles, i.e. 310 years in total, to obtain a quasi-equilibrium state (Danek et al., 2019). The first cycle was initialized from the PHC3 dataset (Steele et al., 2001) and the subsequent cycles were initialized from the last time step of the previous cycle. All analyses are based on the fifth, i.e. last, cycle.

To analyze the resolution-dependence of the involved dynamical processes during MLD restratification, low- and high-resolution FESOM grids were designed (Fig. 1). Based on a global average horizontal resolution of 130 (40) km, the element size was reduced to 40 (20) km along the coasts and the equator in the low (high) -resolution setup to improve the modeling of upwelling. Upon this, the resolution was further increased in the subpolar gyre, the Arctic Ocean, deep convection areas and along the Greenland coast. The low-resolution grid (39 vertical levels) was utilized in earlier FESOM experiments and showed good agreement with the LS deep water variability compared to observations, albeit missing fluxes between the boundary current and the LS interior (Scholz et al., 2014). In the high-resolution setup (61 vertical levels) the element size was further reduced in the North Atlantic where measured (1) SSH variability is high (AVISO), (2) bottom slopes are steep (Amante and Eakins, 2009) and (3) horizontal temperature gradients in 200 m depth are large (Locarnini et al., 2013). With these constraints we ensured an appropriate representation of important dynamic processes related to mesoscale eddies, fronts, boundary currents, upwelling, and topographic features. As discussed

later, the obtained ~ 5 km horizontal resolution render the applied SGS fluxes negligible in the high-resolution setup due to its scaling with the local horizontal resolution (Figs. 5b, c and 6).

2.2. Eddy temperature fluxes and eddy kinetic energy

The Boussinesq tendency equation for depth-integrated potential temperature T in flux form (in $^\circ\text{C m s}^{-1}$) can be written as

$$\partial_t \int T dz = - \int \nabla \cdot (\mathbf{u} + \mathbf{u}_{\text{SGS}})T dz + F + \text{Rest} \quad (1)$$

with ∂_t being the partial derivative with respect to time, z the vertical coordinate and ∇ , \mathbf{u} and \mathbf{u}_{SGS} the three-dimensional spatial derivative, velocity and SGS velocity vectors. The first term on the right hand side of Eq. (1) represents the temperature advection divergence. As any vector transport may be separated in a divergent and a rotational component, $\mathbf{u}T = (\mathbf{u}T)_D + (\mathbf{u}T)_R$ (Helmholtz theorem) (Zdunkowski and Bott, 2003), using the flux form here is advantageous since the rotational part of the vector field does not affect the dynamics of the flow (Marshall and Shutts, 1981; Jayne and Marotzke, 2002; Fox-Kemper et al., 2003), and, by definition, the rotational part is divergence-free ($\nabla \cdot (\mathbf{u}T)_R = 0$). Hereafter, we refer to convergence instead of divergence so that a positive convergence $-\nabla \cdot \mathbf{u}T$ yields a temperature increase. The second term in Eq. (1) represents the thermodynamic boundary condition at the sea surface $F = (\rho c_p)^{-1} Q_{\text{net}}$ with surface density ρ and the specific heat capacity of sea water at constant pressure c_p , for which we used a constant value close to the average of today's global ocean surface (3991.867 957 119 63 m² s⁻² K⁻¹, IOC, SCOR, IAPSO, 2010). The net surface heat flux Q_{net} was calculated during model runtime via bulk formulae based on the individual heat flux components of the CORE-II forcing (Large and Yeager, 2009). All other components are subsumed in the Rest term, e.g. diffusion and non-local transports through the KPP vertical mixing scheme (Large et al., 1994).

To distinguish between temperature fluxes from long and short time scales, Reynolds averaging (Vallis, 2017) of the horizontal advection term yields

$$-\nabla_h \cdot (\overline{\mathbf{u}_h + \mathbf{u}_{\text{SGS},h}} \overline{T}) = -\nabla_h \cdot (\overline{\mathbf{u}_h} \overline{T} + \overline{\mathbf{u}'_h T'} + \overline{\mathbf{u}_{\text{SGS},h}} \overline{T}) \quad (2)$$

where the subscript h indicates the horizontal component of a vector, the overbar a temporal mean and the prime a deviation from that mean. Following von Storch et al. (2012), we derive the eddy temperature flux $\overline{\mathbf{u}'T'}$ by calculating the total temperature flux $\mathbf{u}T$ in every model time step and save its monthly mean $\overline{\mathbf{u}T}$. As such, seasonal and longer time scales are part of the mean term while $\overline{\mathbf{u}'T'}$ represents deviations on temporal scales from the model time step to a month without the necessity of saving large high-resolution 3D model data on a high temporal frequency. Fig. 2 confirms that similar monthly mean eddy fluxes are obtained with this method, independent of the model output frequency.

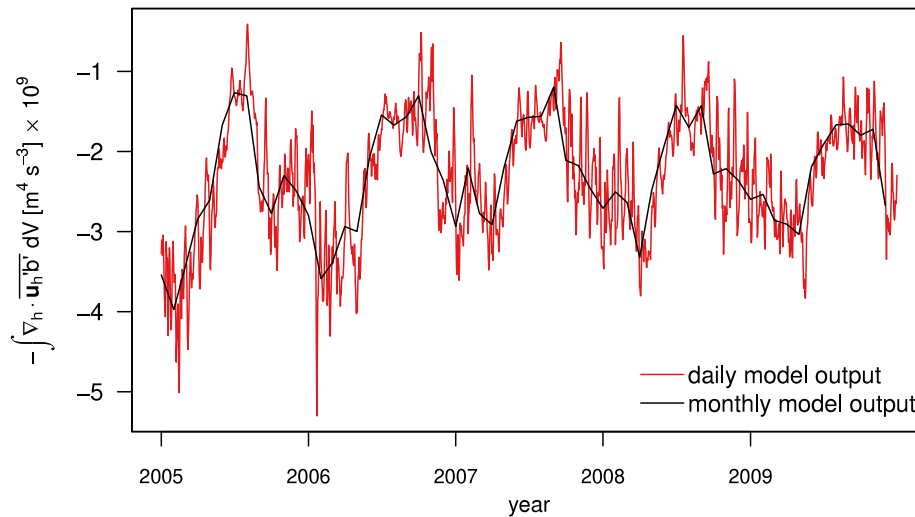


Fig. 2. Eddy component of horizontal buoyancy advection convergence volume-integrated over a box located at Fram Strait (-20 to 20°E , 76 to 82°N) calculated based on monthly (black) or daily (red) model output (larger values indicate buoyancy gain in summer; see methods section for eddy component calculation). Model data taken from another FESOM run with the same model version, parameters and forcing as in this study (Wekerle et al., 2017).

To identify the sources and sinks of $\text{EKE} = \mathbf{u}_h'^2/2$ (neglecting vertical velocity w due to hydrostatic approximation), the Lorenz Energy Cycle (Lorenz, 1955) can be applied (Böning and Budich, 1992; Marchesiello et al., 2003; von Storch et al., 2012; Renault et al., 2016). The volume-integrated EKE tendency equation, derived from the hydrostatic Boussinesq momentum balance (from Section 12.2 in Olbers et al., 2012)

$$\partial_t \int \text{EKE} dV = \int (F_e K_e + \text{drag}) dA + \int (K_m K_e + P_e K_e + \text{dissipation}) dV \quad (3)$$

yields the individual energy conversion terms which change EKE during instability processes and associated interactions with the mean flow (integrated over volume V or area A ; in $\text{m}^5 \text{s}^{-3}$). $F_e K_e = \rho_0^{-1} (\mathbf{u}_h' \cdot \boldsymbol{\tau}')$ represents eddy growth through work of wind anomalies at the sea surface via wind stress $\boldsymbol{\tau}$ (in $\text{kg m}^{-1} \text{s}^{-2}$) and can be understood as a mechanical source of instability by the atmospheric forcing. Vice versa, bottom drag $= -C_d |\mathbf{u}_h'| \mathbf{u}_h' \cdot \mathbf{u}_h'$ leads to EKE removal, scaled by the dimensionless bottom friction coefficient $C_d = 0.0025$. The transfer from mean to eddy kinetic energy due to barotropic instabilities $K_m K_e = \text{HRS} + \text{VRS}$, i.e. the sum of horizontal and vertical Reynolds stresses. They let eddies grow or decay due to horizontal and vertical shear: $\text{HRS} = -\overline{u'^2 \partial_x \bar{u}} - \overline{u'v' \partial_y \bar{u}} - \overline{u'v' \partial_x \bar{v}} - \overline{v'^2 \partial_y \bar{v}}$ and $\text{VRS} = -\overline{u'w' \partial_z \bar{u}} - \overline{v'w' \partial_z \bar{v}}$. As such, VRS represents Kelvin–Helmholtz instability. The vertical eddy buoyancy flux $P_e K_e = \overline{w'b'}$ with buoyancy $b = -g\rho_0^{-1} \rho$ is indirectly related to baroclinic instability through the exchange between turbulent potential and kinetic energy. EKE dissipation $= -A_v |\partial_z \mathbf{u}_h'|^2$ by small-scale turbulence is implemented in the model via vertical viscosity (or momentum diffusivity) A_v (in $\text{m}^2 \text{s}^{-1}$). Here, this dissipation term is calculated as the residual of the left hand side and all other terms of Eq. (3). In the following, these energy conversion terms are defined such that if positive, EKE is generated at the expense of the mean flow. In turn, if negative, EKE is transferred back to the mean flow (or dissipated) by turbulence.

3. Results

3.1. Labrador Sea temperature fluxes

On average (1948–2009) the Labrador Sea (LS) is losing heat to the atmosphere through outgoing longwave radiation and sensible and latent heat fluxes ($F < 0$; shading in Fig. 3a, b). This heat loss is partly compensated by the boundary current. The depth-integrated horizontal mean temperature flux convergence exhibits large values

along the West Greenland Current (WGC; black arrows in Fig. 3c, d). In the high-resolution run (~ 5 km local horizontal resolution) heat is mainly provided by the WGC in a narrow band between the 2 and 3 km isobaths, while being removed on- and off-shore of this patch. This spatial tripole was also seen in earlier studies (Kawasaki and Hasumi, 2014; Tagklis et al., 2020). The heat supply continues along the 3 km isobath. Further downstream, a second route of large heat supply establishes at $\sim 62.5^\circ$ that continues along the 2 km isobath throughout the LS in accordance with de Jong et al. (2016), Tagklis et al. (2020). The structure of the low-resolution (~ 20 km local horizontal resolution) boundary current is broader and more homogeneous as in the high-resolution setup and provides heat in a large patch between the 2 and 3 km isobaths (Fig. 3c). Heat is lost on the onshore side of this temperature convergence, yielding a large-scale dipole pattern in contrast to the numerous convergence/divergence patches of the high-resolution mean temperature fluxes along the boundary current. In the LS interior, the mean temperature advection convergence is ~ 1 magnitude smaller compared to the boundary current region in both model setups. Here, divergent and convergent patches coexist next to each other. This feature is much more heterogeneous in the high-resolution model with a large number of divergent and convergent patches on spatial scales of tens to a few hundreds of km. The low-resolution LS interior is gaining (losing) heat in the northeast (southwest) due to the average circulation.

The depth-integrated temperature flux fluctuations on temporal scales from the model time step to a month (i.e. eddy component; see methods) follow the main circulation around the LS, similarly as the mean component but is ~ 1 magnitude smaller (Fig. 3e, f). This in contrast to earlier studies (Chanut et al., 2008; Saenko et al., 2014; Kawasaki and Hasumi, 2014; de Jong et al., 2016; Tagklis et al., 2020) and will be discussed later. As a consequence, the total advection (mean + eddy, Fig. 4) resembles the mean component. The heat supply and removal by the mean circulation is generally enforced by the eddy fluxes in the high-resolution setup (same sign). This is not the case in the northern part of the LS interior as well as further downstream along the 3 km isobath, where mean and eddy fluxes mostly compensate, in agreement with these studies. The low-resolution eddy fluxes occur in broader spatial patterns compared to the high-resolution setup. Regions of compensating (e.g. between 1 and 2 km isobaths, partly between 2 and 3 km isobaths) and enforcing (e.g. LS interior) mean and eddy fluxes exist, similarly as in the high-resolution run. The following temporal perspective of the LS dynamics provides further information on the role of the eddy temperature flux component.

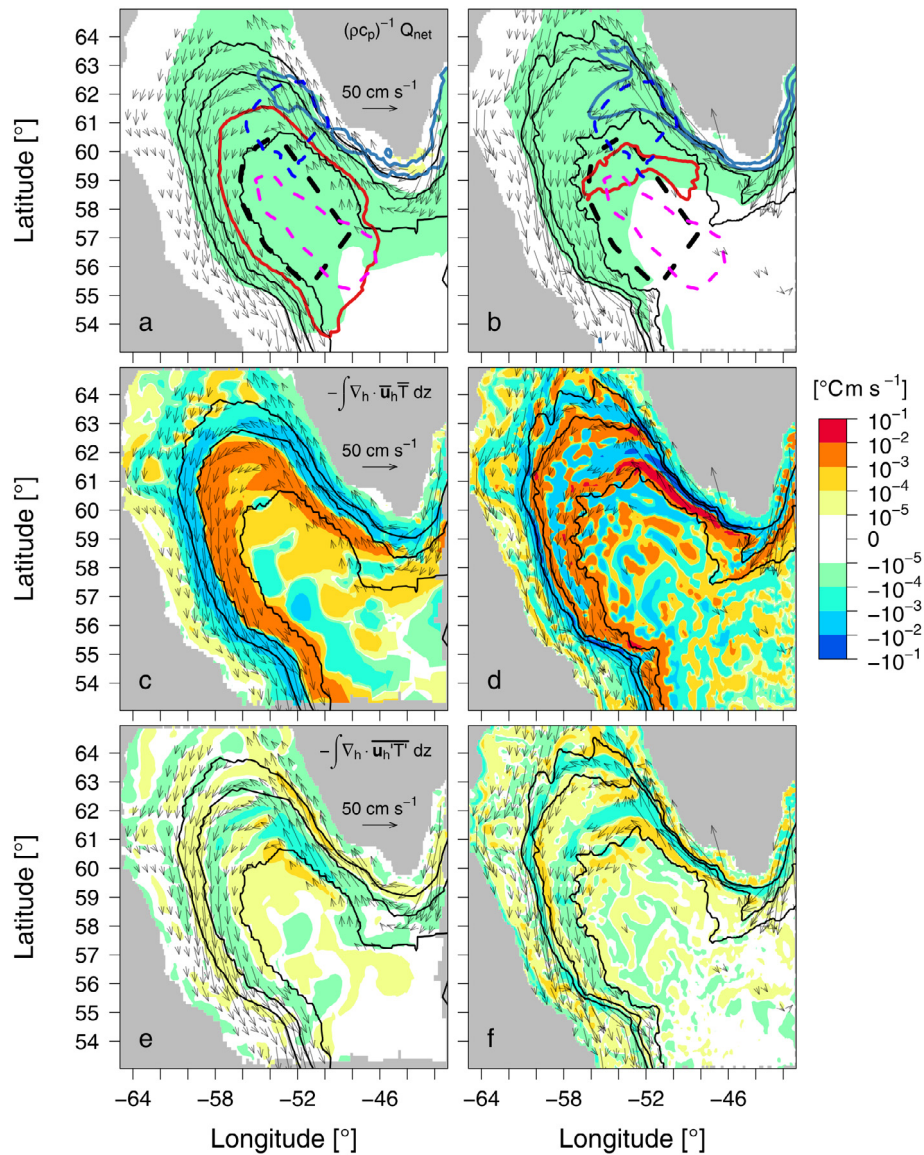


Fig. 3. Average (1948–2009) local temperature changes for low- (left) and high-resolution (right) FESOM setups in the Labrador Sea. (a, b) Surface flux $(\rho c_p)^{-1} Q_{net}$, (c, d) mean $-\nabla_h \cdot \bar{u}_h \bar{T}$, and (e, f) eddy $-\nabla_h \cdot \bar{u}_h \bar{T}'$ depth-integrated horizontal temperature advection convergence (positive values indicate temperature gain). In (a, b), dashed black lines show the LS interior index region, solid and dashed blue lines the modeled and observed (satellite altimetry) isolines of the individual means plus two standard deviations of EKE, and solid red and dashed magenta lines the modeled and observed (EN4, Good et al., 2013) 2 km MLD (March; σ_θ threshold 0.125 kg m^{-3}). Arrows show sea surface velocity direction and magnitude greater or equal 5 cm s^{-1} and black contours the 1, 2 and 3 km isobaths.

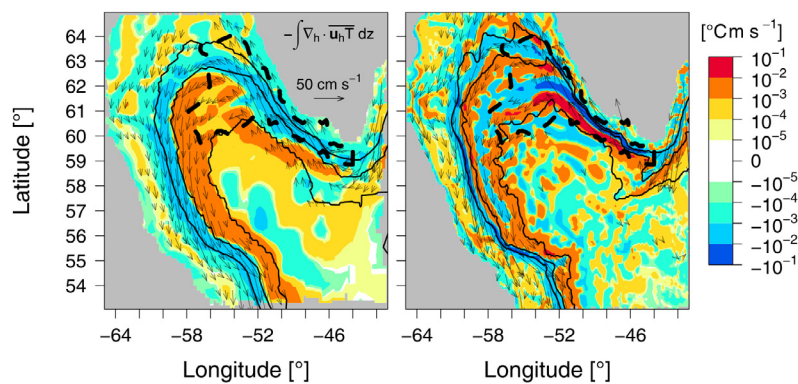


Fig. 4. Average (1948–2009) local temperature changes for low- (left) and high-resolution (right) FESOM setups in the Labrador Sea due to depth-integrated total (mean + eddy) horizontal temperature advection convergence $-\nabla_h \cdot \bar{u}_h \bar{T}$ (positive values indicate temperature gain; same colorbar as in Fig. 3). Dashed black lines show the index region of the WGC and its separation from the coast (defined where high-resolution HRS and $P_e K_e$ exhibit large values, Fig. 7d, f). Arrows show sea surface velocity direction and magnitude greater or equal 5 cm s^{-1} and solid black the 1, 2 and 3 km isobaths.

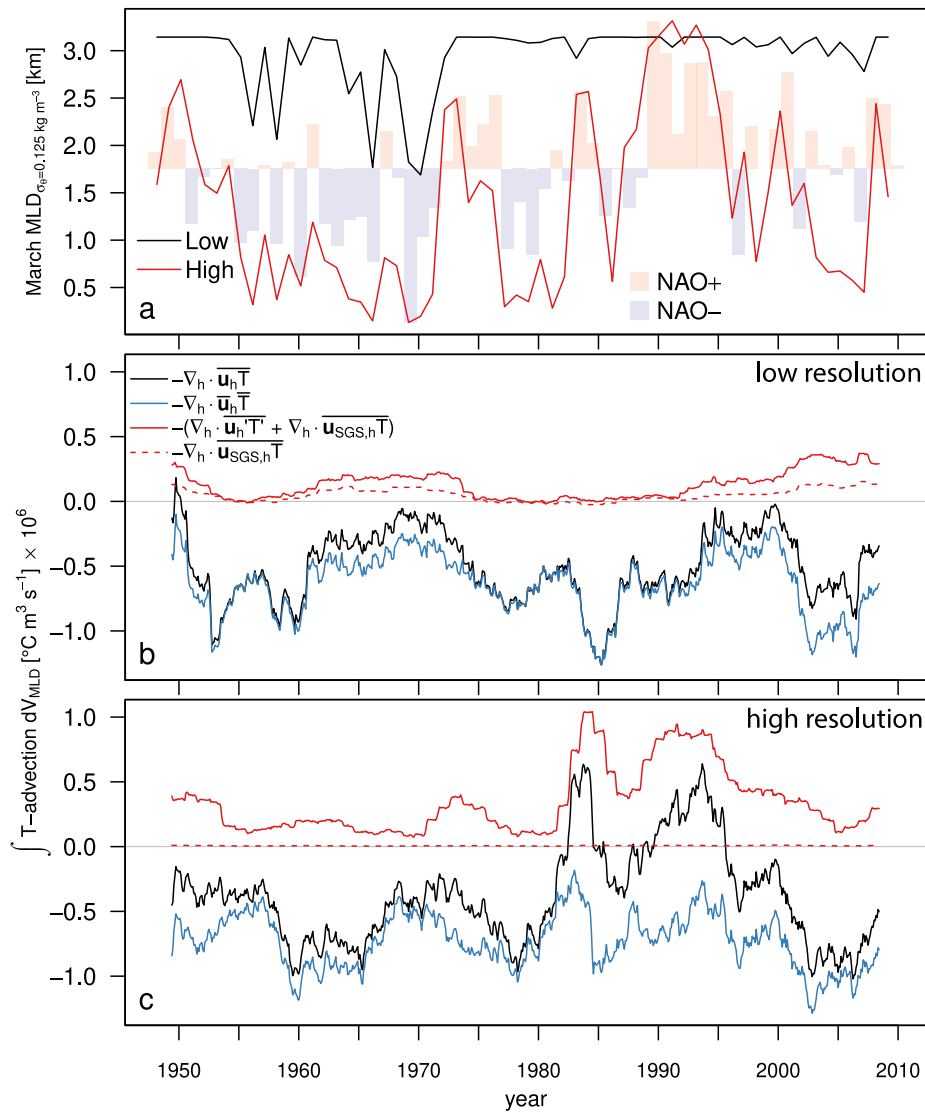


Fig. 5. (a) March MLD of low- (black) and high-resolution (red) FESOM setups (in km; σ_{θ} threshold 0.125 kg m^{-3}). (b) and (c) Low- and high-resolution total horizontal temperature advection convergence $-\nabla_h \cdot \bar{\mathbf{u}}_h \bar{T}$ (black lines) integrated over the LS interior (dashed black line in Fig. 3a, b) from the surface to the mixed layer depth (positive values indicate temperature gain). Components: mean $-\nabla_h \cdot \bar{\mathbf{u}}_h \bar{T}$ (blue), combined eddy and SGS $-(\nabla_h \cdot \bar{\mathbf{u}}_h \bar{T}' + \nabla_h \cdot \bar{\mathbf{u}}_{SGS,h} \bar{T})$ (red), SGS $-\nabla_h \cdot \bar{\mathbf{u}}_{SGS,h} \bar{T}$ (dashed red). A 3-year running mean is applied to all advection convergence time series. In (a), red (blue) bars in background indicate years with a positive (negative) PC-based NAO index (Hurrell, 2003).

In the LS interior, atmospheric forcing triggers deep convection events throughout the observational period (Fig. 5a). In positive NAO years (North Atlantic Oscillation, Hurrell, 2003), an increased oceanic heat loss to the atmosphere yields a deep mixed layer depth (MLD), here defined as the depth at which the potential density σ_{θ} deviates from its 10 m depth value by 0.125 kg m^{-3} (Danabasoglu et al., 2014), of several km during winter (deepest in March in both model setups, not shown). The decadal evolution of the March MLD reveals pronounced differences between the low- and high-resolution model runs. While the high-resolution MLD is in phase with the NAO, the low-resolution model exhibits almost no temporal variability and remains at deep depths (Fig. 5a; averaging area outlined by dashed black line Fig. 3a, b). In addition, the average March low-resolution MLD spans a much larger area compared to the high-resolution setup and observations (EN4, Good et al., 2013). Other MLD thresholds do not change these general differences between the model setups and observations (not shown).

A similar picture emerges for the horizontal eddy temperature advection convergence, volume-integrated from the surface to the respective MLDs within the LS interior (index area shown by dashed black line in Fig. 3a, b). While the large-scale circulation leads to heat loss

in the convection zone, high-resolution eddy fluxes temporarily become active and reduce or even balance this heat loss during deep convection events (red line in Fig. 5c). These dynamics are almost absent in the low-resolution model, where the eddy contribution is much weaker and hardly balances the heat loss due to the mean circulation (Fig. 5b). Here, subgrid-scale (SGS) fluxes are strongly enhanced compared to the negligible values of the high-resolution model (dashed red lines in Fig. 5b, c). However, the total temperature advection convergence including the SGS contribution remains negative in the low-resolution mixed layer. Integration over the whole water column suggests an important stabilizing contribution of the mean circulation below the mixed layer (Fig. 6). Here, mean and eddy temperature advection components compensate the heat loss from the atmospheric forcing, yielding a dynamical equilibrium in the high-resolution run (close agreement between left and right hand sides of Eq. (1); orange and gray lines in Fig. 6 bottom). This equilibrium is not obtained in the low-resolution run, where the eddy contribution is too weak and the mean circulation does not work against the forcing (Fig. 6 top). The resulting imbalance needs to be closed by horizontal and vertical diffusion including the lon-local transport term from the KPP parameterization

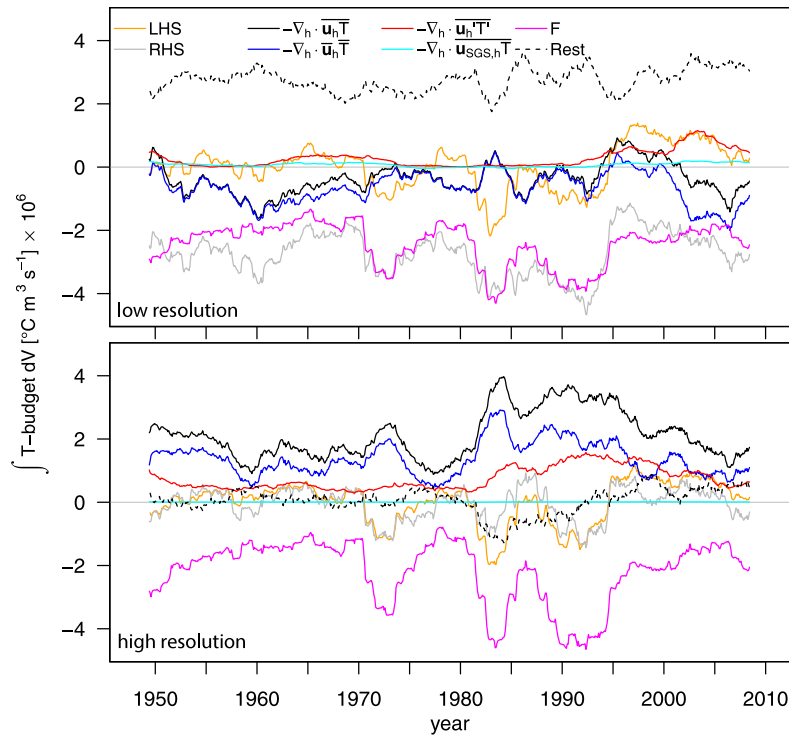


Fig. 6. Contributions to temperature changes volume-integrated over the Labrador Sea interior (dashed black line in Fig. 3a, b) in low- (top) and high-resolution (bottom) model runs. Components (Eq. (1)): mean $-\nabla_h \cdot \mathbf{u}_h \overline{T}$ (blue), eddy $-\nabla_h \cdot \mathbf{u}'_h \overline{T'}$ (red), total $-\nabla_h \cdot \mathbf{u}_h \overline{T}$ (mean+eddy; black) and SGS $-\nabla_h \cdot \mathbf{u}_{\text{SGS},h} \overline{T}$ (cyan) temperature advection convergence as well as the area-integrated atmospheric forcing F (magenta). The sum of the latter three is shown as RHS (gray) while the actual model solution of $\partial_t T$ is shown as LHS (orange). The difference LHS minus RHS is shown as Rest (dashed black). Positive values indicate temperature gain. A 3-year running mean is applied to all time series.

as well as the vertical component of advection and the parameterized SGS flux (dashed black lines in Fig. 6).

3.2. EKE generation in the Labrador Sea

The spatial structure of the annual average surface Eddy Kinetic Energy (EKE) follows the WGC and its separation from the coast as shown by the blue isolines of the individual means plus two standard deviations in Fig. 3a, b. Their numerical values are 124 and $257 \text{ cm}^2 \text{ s}^{-2}$ for the low- and high-resolution model runs (solid blue lines) and $39 \text{ cm}^2 \text{ s}^{-2}$ for satellite altimetry (1993 to 2009; dashed blue line). EKE values are twice as large and reach far more into the LS interior in the high- compared to the low-resolution run. The observed spatial EKE structure is more similar to the high-resolution setup. In addition, enhanced EKE values are found south of the 3 km isobath, which is not the case in both model runs. Absolute values of EKE derived from altimetry are much lower than the modeled EKE due to the inference from geostrophic currents excluding the ageostrophic component based on daily snapshots excluding variability on shorter time scales on relatively coarse 0.25° horizontal resolution (Rieck et al., 2019). The spatial structure of the modeled depth-integrated EKE similarly follows the WGC and its separation from the coast as shown by the solid and dashed blue isolines in Fig. 7a, b (5 and $20 \text{ m}^3 \text{ s}^{-2}$). The $5 \text{ m}^3 \text{ s}^{-2}$ EKE patch is much larger in the high- compared to the low-resolution model run; higher values such as $20 \text{ m}^3 \text{ s}^{-2}$ are not reached by the latter. On average, the depth-integrated EKE peaks in March (Fig. 9e). Hence, EKE generating processes will be analyzed for this month.

In March EKE is generated through turbulent wind work ($F_e K_e > 0$) at the sea surface with larger values in the eastern part of the LS (Fig. 7a, b). The rather homogeneous spatial pattern of EKE generation through $F_e K_e$ reflects that on average the wind stress and surface current anomalies point into the same direction, in line with previous studies (von Storch et al., 2007; von Storch et al., 2012; Rimac et al., 2016). The depth-integrated barotropic HRS leads to eddy growth at

the expense of the mean flow on the offshore side of the WGC, before and after separation from the Greenland coast (Fig. 7c, d). In a narrow patch between the 1 and 2 km isobaths along the coasts of Greenland and Canada, eddies transfer energy back the mean flow by horizontal shear ($\text{HRS} < 0$). The high-resolution run exhibits much larger values of this barotropic instability compared to the low-resolution setup. These large HRS values drop by ~ 2 magnitudes towards the LS interior. Depth-integrated baroclinic instability $P_e K_e$ is responsible for an EKE increase almost everywhere in the LS (Fig. 7e, f). Its general pattern resembles the barotropic one with enhanced values along the WGC and the downstream circulation. As expected, the region of large depth-integrated HRS and $P_e K_e$ corresponds with the depth-integrated EKE (blue isolines in Fig. 7a, b).

Wind forcing is a constant source of EKE (solid lines and left axis in Fig. 8a) with decadal fluctuations smaller than the average seasonal cycle (Fig. 9a). Area-integrated over the LS interior, both model setups exhibit similar $F_e K_e$ values with small differences probably arising from faster surface currents in the high-resolution run. Volume-integrated barotropic and baroclinic EKE conversion terms, in contrast, differ greatly between low- and high-resolution runs (solid lines and left axes in Fig. 8b, c). During deep convection events in the early 1970s, mid-1980s and early to mid-1990s, high-resolution barotropic and baroclinic instabilities are strongly enhanced in the LS interior. Negative HRS and VRS lead to a removal of EKE in the LS interior (note the smaller order of magnitude for VRS; dashed lines and right axis in Fig. 8b). However, eddy growth in the LS interior due to baroclinic instabilities $P_e K_e$ is one magnitude larger than the combined barotropic instabilities $K_m K_e$ (this is also the case in the area of the WGC and its separation from the coast, Fig. 10). Hence, the evolution of the volume-integrated EKE closely follows $P_e K_e$ (dashed lines and right axis in Fig. 8c). Similar proportions apply to the low-resolution run (although much reduced in absolute numbers) and to the average seasonal cycle (Fig. 9b-e). EKE is removed mainly by dissipation through vertical momentum diffusion and, by a much smaller amount, bottom drag

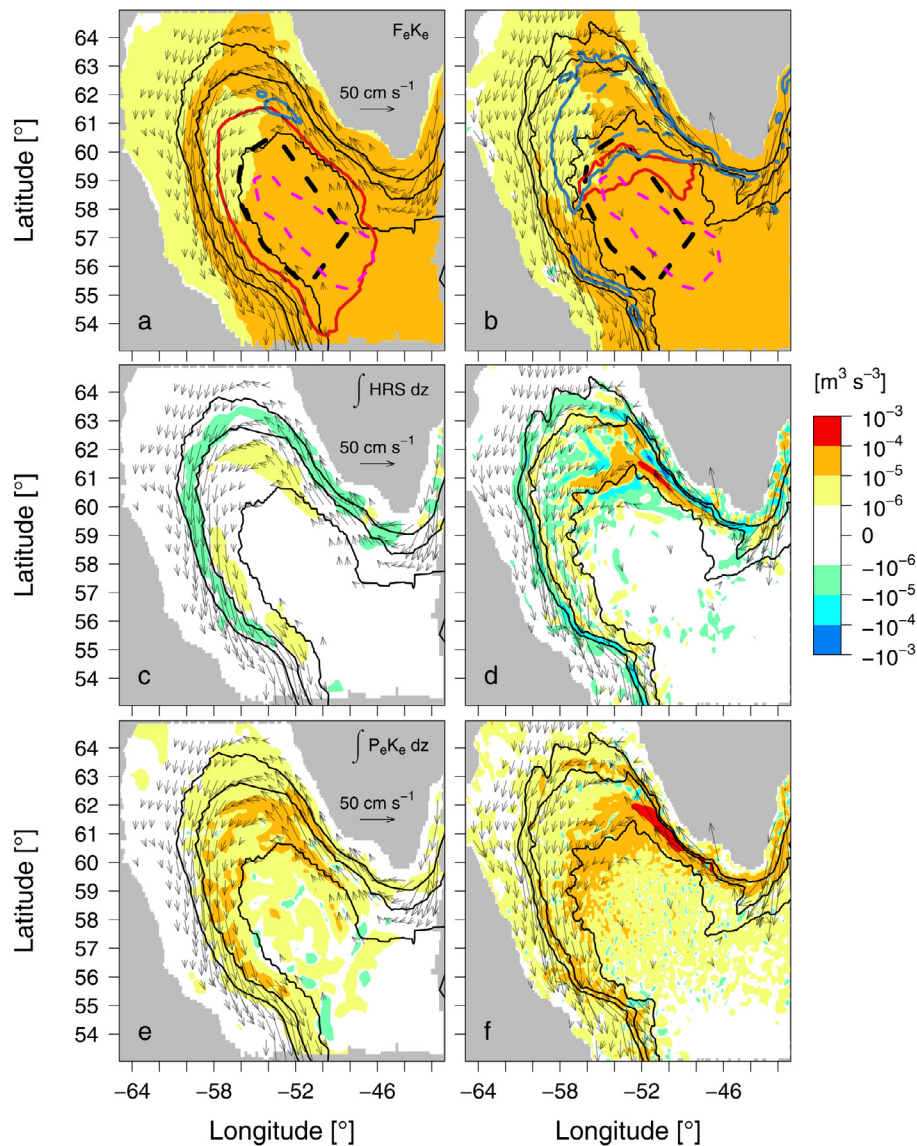


Fig. 7. Average (1948–2009, March) local EKE changes of low- (left) and high-resolution (right) FESOM setups in the Labrador Sea. (a, b) Eddy wind work at the sea surface $F_e K_e$. Solid red and dashed magenta contours show the modeled and observed (EN4, Good et al., 2013) 2 km MLD (σ_θ threshold 0.125 kg m^{-3}), blue contours the depth-integrated 5 (solid) and 20 (dashed) $\text{m}^3 \text{ s}^{-2}$ EKE and thick dashed black lines the LS interior index region. (c, d) Horizontal barotropic HRS and (e, f) baroclinic $P_e K_e$ instabilities (depth-integrated; positive values indicate EKE generation). Arrows show sea surface velocity direction and magnitude greater or equal 5 cm s^{-1} and black contours the 1, 2 and 3 km isobaths.

(Fig. 11). The EKE contribution to the total kinetic energy $u_h^2/2$ does not show pronounced peaks during deep water formation events but rather stays around 25% in the low- and around 45% in the high-resolution run (dashed lines and right axis in Fig. 8a). Their decadal fluctuations are of similar magnitude as the average seasonal cycle (Fig. 9f).

4. Discussion

The Labrador Sea as modeled with FESOM exhibits a vivid EKE field with a pronounced decadal variability. At a local horizontal resolution of $\sim 5 \text{ km}$, this turbulence is strong enough to induce small-scale temperature fluxes that lead to an efficient MLD restratification (Fig. 5). At a slightly decreased local resolution of $\sim 20 \text{ km}$, these fluxes are too weak to increase stability (parameterized SGS fluxes taken into account) and the resulting MLD is too deep and its extent too large - a common problem of state-of-the-art ocean and climate models (Danabasoglu et al., 2014; Heuzé, 2021; Koenigk et al., 2021).

In the LS interior, the modeled turbulence is mostly of baroclinic origin induced through upward eddy buoyancy fluxes (Fig. 8). Our results thus support the view that meso- to submesoscale baroclinic instabilities are essential for restratifying the water column after convection. Baroclinic instability induced through large ageostrophic velocities (Lavender et al., 2002) transport heat upwards (Morrison et al., 2013; Saenko, 2015) that draws turbulent potential energy from steep isopycnals, which thereby flatten (Fox-Kemper et al., 2008). The large interannual variability of this upward eddy buoyancy flux dominates the temporal evolution of the volume-integrated EKE (Fig. 8c), indicative of important subsurface EKE generation (Hu et al., 2020). Hence, reported non-significant surface EKE trends of the highly baroclinic and eddy-rich Gulf Stream and Kuroshio current derived from satellite altimetry may be underestimated (Martínez-Moreno et al., 2021).

In the area of the WGC and its separation from the coast, barotropic instability (mainly horizontal shear) additionally becomes important for eddy growth (Eden and Böning, 2002) but turbulent buoyancy fluxes remain the dominant EKE source (Fig. 10), in line with previous

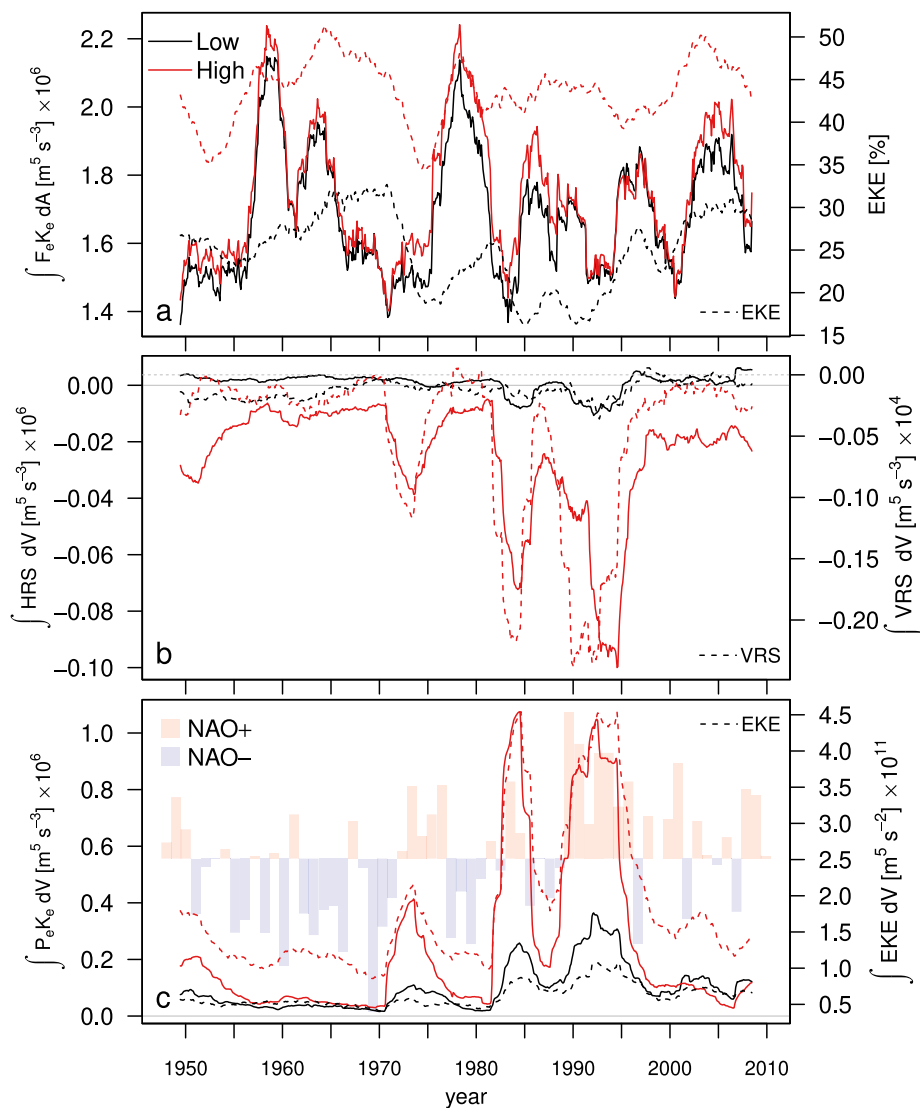


Fig. 8. Decadal evolution of low- (black) and high-resolution (red) EKE changes due to (a) area-integrated eddy wind work at the sea surface $F_e K_e$, (b) horizontal barotropic HRS and (c) baroclinic $P_e K_e$ volume-integrated instabilities in the LS interior (dashed black line in Fig. 3a, b; left axes; positive values indicate EKE generation). Dashed lines (right axes) show EKE contribution to total kinetic energy (a), volume-integrated vertical barotropic instabilities VRS (two orders of magnitude smaller than the other EKE conversions; b) and EKE (c). A 3-year running mean is applied to all time series. In (c), red (blue) bars in background indicate years with a positive (negative) PC-based NAO index (Hurrell, 2003).

studies (Saenko et al., 2014; Pacini and Pickart, 2022). Observations indicate that eddies generated within and advected with the boundary current transport heat and salt (or freshwater) into the LS interior (Irving Rings) (Jones and Marshall, 1997; Lilly et al., 2003; Straneo, 2006; Schmidt and Send, 2007; Rykova et al., 2009; de Jong et al., 2014; Rykova et al., 2015). This implies that the seawater properties of the boundary current set the restratification ability of the eddies. We can confirm this since the efficient MLD restratification seen in our high-resolution setup was only achieved when the boundary current was not biased too dense and thus being able to provide buoyant water masses (i.e. after some forcing cycles, Danek et al., 2019). Hence, if no buoyant water is available in the interior or the boundary current, upward turbulent buoyancy fluxes as well as eddies from the WBC may not contribute to restratification (Thomas and Zhang, 2022). This view is supported by observations (Luo et al., 2012; Pacini and Pickart, 2022) and model results where a suppressed turbulence in the WGC led to an underestimation of transports of heat into the LS interior by Irving Rings and a deeper MLD (Gelderloos et al., 2011; Kawasaki and Hasumi, 2014; Rieck et al., 2019; Pennelly and Myers, 2022).

Previous studies using realistic high-resolution ocean models found that on the long-term average, mean and eddy temperature flux convergence are of equal importance in the LS (Chanut et al., 2008; Saenko et al., 2014; Kawasaki and Hasumi, 2014; de Jong et al., 2016; Tagklis et al., 2020). Common to some of these studies is an eddy definition that incorporates deviations from a relatively long period, e.g. 5 (Chanut et al., 2008; Saenko et al., 2014), 7 (Tagklis et al., 2020) or 14 years (de Jong et al., 2016). Our eddy component, in contrast, represents fluctuations on much shorter time scales from the model time step to a month (von Storch et al., 2012). We thereby provide another perspective on the mean/eddy interplay: on the long-term average (1948–2009), the eddy temperature fluxes are much weaker than the mean component, also in the high-resolution setup, whereby the total advection resembles the mean component (compare Figs. 3c, d and 4). Triggered by strong forcing, however, the eddy component greatly increases, playing a role equally important as the mean circulation, as long as the spatial resolution is high enough which is in accordance with the cited studies above (Figs. 5b, c and 6). Hence, together with the notion that a longer averaging period

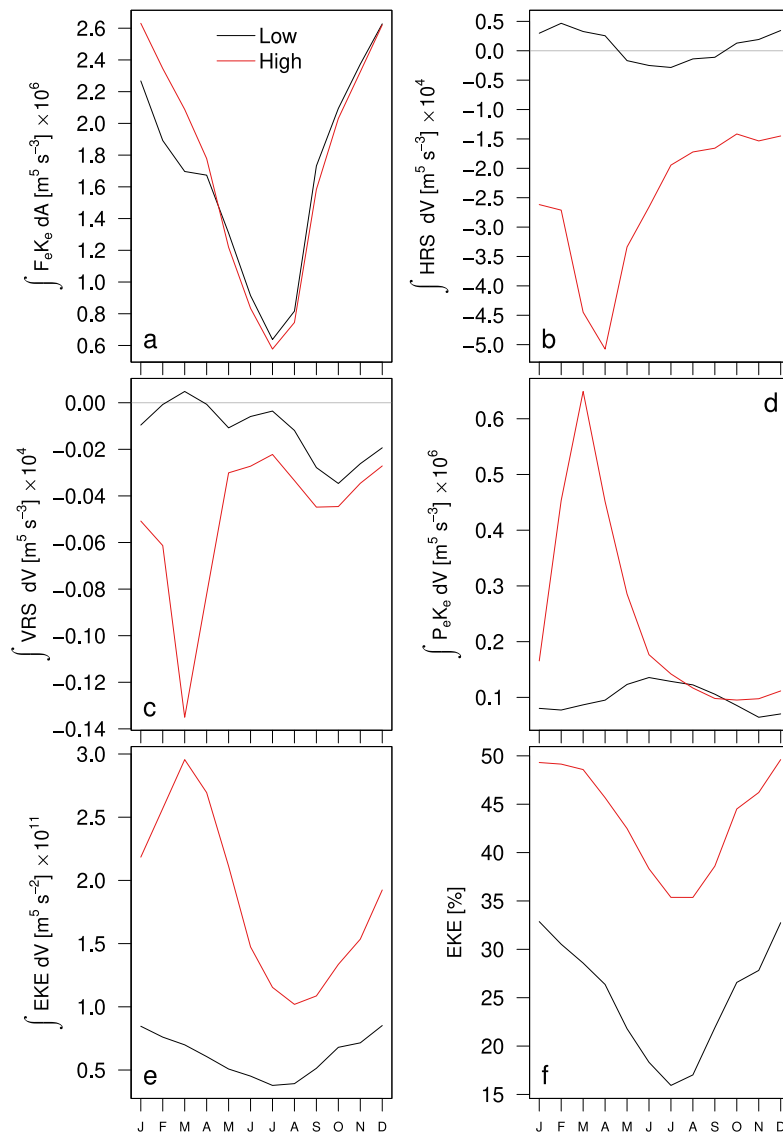


Fig. 9. Average (1948–2009) seasonal cycle of low- (black) and high-resolution (red) EKE changes due to (a) area-integrated eddy wind work at the sea surface $F_e K_e$, (b) horizontal (HRS), (c) vertical barotropic (VRS) and (d) baroclinic $P_e K_e$ volume-integrated instabilities in the LS interior (dashed black line in Fig. 3a, b; positive values indicate EKE generation; different y-axes). (e, f) show the volume-integrated EKE and its contribution to total kinetic energy.

leads to larger deviations from that average (Rieck et al., 2015), this physically consistent picture was not documented earlier due to the missing decadal temporal perspective. In Kawasaki and Hasumi (2014), however, the temporal average of mean and eddy heat flux components are of similar magnitude although the same eddy definition as in this study was used. In contrast to our 62 years of 6-h atmospheric forcing, they utilized a daily climatology representing the years 1979 to 1993 to force their ocean model. This time period is biased towards a positive NAO phase and thus enhanced heat loss in the LS (Röske, 2006). For this period, our high-resolution run indeed shows a similar importance of mean and eddy components of heat fluxes integrated over the mixed layer (Fig. 5b, c) and the whole water column (Fig. 6). Hence, it may be that the heat flux composition presented by Kawasaki and Hasumi (2014) rather represent a positive NAO state and not a general temporal average.

The complex spatial structure of the high-resolution heat flux convergence due to the construction via the divergence operator is difficult to interpret and may require more averaging than applied in this study. For example, spatial smoothing was used to obtain a more coherent picture (Chanut et al., 2008; Saenko et al., 2014). On the other hand,

small-scale features may get lost due to smoothing, as for example the heat loss patch on the onshore side of the WGC due to the mean circulation (Kawasaki and Hasumi, 2014; Tagklis et al., 2020, this study). Another example is the interplay between mean and eddy temperature fluxes in the WGC, which were shown to generally work against each other (opposite sign; Chanut et al., 2008; Saenko et al., 2014; Kawasaki and Hasumi, 2014; de Jong et al., 2016). Our high-resolution eddy temperature fluxes, in contrast, tend to enforce the mean WGC (same sign). This is also seen in Tagklis et al. (2020), where a higher model resolution seems to yield a larger agreement of the signs of mean and eddy flux components over large parts of the WGC within the 2 and 3 km isobaths. Hence, a general relationship between the type of instability and effects of the resulting eddy fluxes, i.e. to enforce or oppose mean fluxes, remains unclear.

Albeit the relatively high spatial resolution the eddy temperature fluxes are not strong enough to efficiently limit the spatial extent of the MLD in the high-resolution setup, especially to the northeast of the deep LS interior where the MLD patch is too large compared to observations (irrespective of MLD threshold). Recent model results suggest that too many vertical model levels (61 in our high-resolution

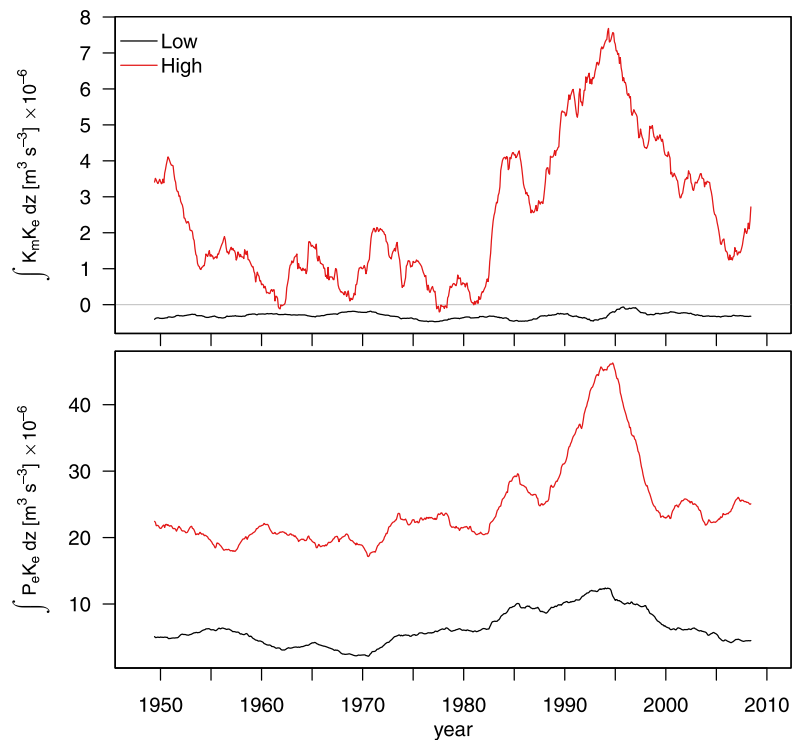


Fig. 10. Decadal evolution of low- (black) and high-resolution (red) EKE changes due to depth-integrated barotropic ($K_m K_e$, top) and baroclinic ($P_e K_e$, bottom) instabilities averaged over the area of the WGC and its separation from the coast (dashed black line in Fig. 4; positive values indicate an EKE generation). A 3-year running mean is applied to all time series.

setup) and a thereby too smooth slope geometry reduces turbulence and hence small-scale tracer fluxes (Gillard et al., 2022). Our low-resolution model reveals further challenges. First, the usually utilized SGS parameterization (Gent and McWilliams, 1990) of eddy fluxes is too weak to mimic meaningful effects of turbulence. Second, in the LS interior, where complicated ocean dynamics and steep topography work in concert, large diapycnal buoyancy fluxes from the vertical mixing scheme and dissipation seem necessary to obtain a dynamical equilibrium (Rest term in Fig. 6). This points to the importance of mixing and non-linearities in the LS interior (Morrison et al., 2013; Griffies et al., 2015; Corre et al., 2020) but is beyond the scope of this study.

5. Concluding remarks

To conclude, eddy fluxes on spatio-temporal scales of a few km from the model time step to a month significantly contribute to tracer advection and facilitate mixed layer restratification in the LS after deep convection events. These eddy fluxes are mainly of baroclinic origin and their interannual variability is coupled to the atmospheric forcing, i.e. turbulence is strongly enhanced during periods of large oceanic heat loss and quiescent otherwise. Buoyant water from the boundary current needs to be available to increase stratification in the LS interior. A higher spatial model resolution clearly improves the spatial-temporal structure of the LS deep convection. In addition, future work should concentrate on the systematic improvement of eddy and mixing parameterizations used in climate models, especially in challenging regions like the Labrador Sea. Moreover, methodological definitions of e.g. spatio-temporal flux decomposition and smoothing techniques and their influence on the physical understanding should be communicated in a clearer way.

CRedit authorship contribution statement

Christopher Danek: Conceptualization, Methodology, Software, Validation, Formal analysis, Investigation, Resources, Data curation,

Writing – original draft, Writing – review & editing, Visualization. **Patrick Scholz:** Conceptualization, Methodology, Software, Resources, Supervision, Project administration. **Gerrit Lohmann:** Conceptualization, Methodology, Resources, Supervision, Project administration, Funding acquisition.

Declaration of competing interest

The authors declare that they have no known competing financial interests or personal relationships that could have appeared to influence the work reported in this paper.

Data availability

Data will be made available on request.

Acknowledgments

This work was funded through the MARUM excellence cluster, Germany “The Ocean Floor – Earth’s Uncharted Interface” and the AWI, Germany through the Helmholtz programme “Changing Earth – Sustaining our Future”. This paper is a contribution to the S2 project (Improved Parameterizations and Numerics in Climate Models) of the Collaborative Research Centre TRR 181 “Energy Transfer in Atmosphere and Ocean” funded by the Deutsche Forschungsgemeinschaft, Germany (DFG, German Research Foundation) - Projektnummer 274762653. We thank Sergey Danilov and Qiang Wang for providing the model code of FESOM1.4 and for in-depth discussions. The model code used in this study and key model data that form the figures are available at <https://zenodo.org/record/4896197>. We thank for the helpful and friendly support of the DKRZ (Deutsches Klimarechenzentrum) computing center. Satellite altimetry products were processed by SSALTO/DUACS and distributed by AVISO+ (<https://www.aviso.altimetry.fr>) with support from CNES.

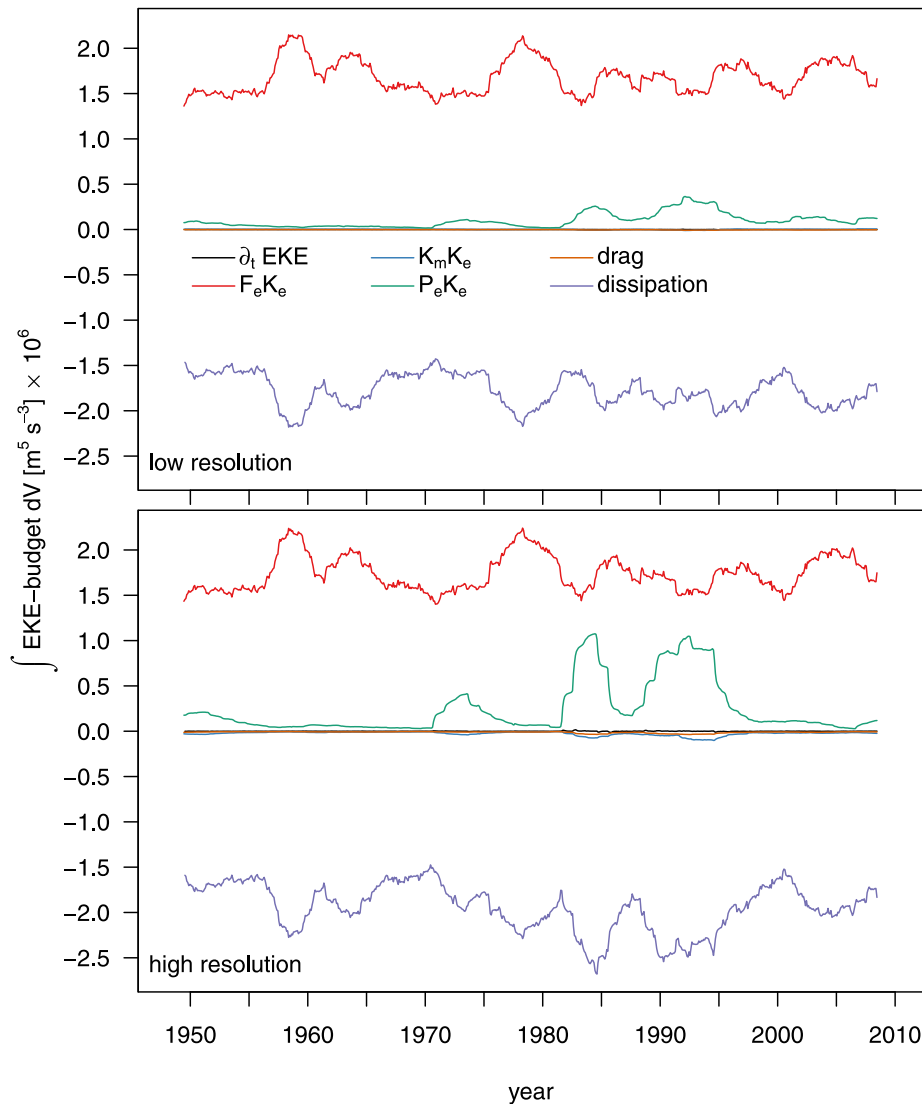


Fig. 11. Decadal evolution of low- (top) and high-resolution (bottom) EKE changes volume- or area-integrated in the LS interior (dashed black line in Fig. 3a, b; positive values indicate EKE generation). Components (Eq. (3)): model solution of ∂_t EKE (black), eddy wind work at the sea surface $F_e K_e$ (red), barotropic $K_m K_e$ (blue) and baroclinic $P_e K_e$ (green) instabilities, bottom drag (orange) and dissipation (purple). A 3-year running mean is applied to all time series.

References

- Amante, C., Eakins, B.W., 2009. ETOPO1 1 Arc-Minute Global Relief Model: Procedures, Data Sources and Analysis. NOAA Technical Memorandum NESDIS NGDC-24, NOAA, [July 15 2015], <http://dx.doi.org/10.7289/V5C8276M>.
- Böning, C.W., Budich, R.G., 1992. Eddy dynamics in a primitive equation model: Sensitivity to horizontal resolution and friction. *J. Phys. Oceanogr.* 22 (4), 361–381. [http://dx.doi.org/10.1175/1520-0485\(1992\)022<0361:ediap>2.0.co;2](http://dx.doi.org/10.1175/1520-0485(1992)022<0361:ediap>2.0.co;2).
- Chanut, J., Barnier, B., Large, W., Debrec, L., Penduff, T., Molines, J.M., Mathiot, P., 2008. Mesoscale eddies in the Labrador Sea and their contribution to convection and restratification. *J. Phys. Oceanogr.* 38 (8), 1617–1643. <http://dx.doi.org/10.1175/2008JPO3485.1>.
- Chelton, D.B., Schlax, M.G., Samelson, R.M., 2011. Global observations of nonlinear mesoscale eddies. *Prog. Oceanogr.* 91 (2), 167–216. <http://dx.doi.org/10.1016/j.pocean.2011.01.002>.
- Corre, M.L., Gula, J., Tréguier, A.-M., 2020. Barotropic vorticity balance of the north atlantic subpolar gyre in an eddy-resolving model. *Ocean Sci.* 16 (2), 451–468. <http://dx.doi.org/10.5194/os-16-451-2020>.
- Danabasoglu, G., Yeager, S.G., Bailey, D., Behrens, E., Bentsen, M., Bi, D., Biastoch, A., Böning, C., Bozec, A., Canuto, V.M., Cassou, C., Chassignet, E., Coward, A.C., Danilov, S., Diansky, N., Drange, H., Farneti, R., Fernandez, E., Fogli, P.G., Forget, G., Fujii, Y., Griffies, S.M., Gusev, A., Heimbach, P., Howard, A., Jung, T., Kelley, M., Large, W.G., Leboissetier, A., Lu, J., Madec, G., Marsland, S.J., Masina, S., Navarra, A., Nurser, A.G., Pirani, A., y Mélia, D.S., Samuels, B.L., Scheinert, M., Sidorenko, D., Treguier, A.-M., Tsujino, H., Uotila, P., Valcke, S., Voldoire, A., Wang, Q., 2014. North Atlantic simulations in Coordinated Ocean-ice Reference Experiments phase II (CORE-II). Part I: Mean States. *Ocean Model.* 73, 76–107. <http://dx.doi.org/10.1016/j.ocemod.2013.10.005>.
- Danek, C., Scholz, P., Lohmann, G., 2019. Effects of high resolution and spinup time on modeled North Atlantic circulation. *J. Phys. Oceanogr.* 49 (5), 1159–1181. <http://dx.doi.org/10.1175/JPO-D-18-0141.1>.
- Danilov, S., Kivman, G., Schröter, J., 2004. A finite-element ocean model: principles and evaluation. *Ocean Model.* 6 (2), 125–150. [http://dx.doi.org/10.1016/S1463-5003\(02\)00063-X](http://dx.doi.org/10.1016/S1463-5003(02)00063-X).
- de Jong, M.F., Bower, A.S., Furey, H.H., 2014. Two years of observations of warm-core anticyclones in the Labrador Sea and their seasonal cycle in heat and salt stratification. *J. Phys. Oceanogr.* 44 (2), 427–444. <http://dx.doi.org/10.1175/JPO-D-13-070.1>.
- de Jong, M.F., Bower, A.S., Furey, H.H., 2016. Seasonal and interannual variations of irmering ring formation and boundary–interior heat exchange in FLAME. *J. Phys. Oceanogr.* 46 (6), 1717–1734. <http://dx.doi.org/10.1175/JPO-D-15-0124.1>.
- Dukhovskoy, D.S., Myers, P.G., Platov, G., Timmermans, M.-L., Curry, B., Proshutinsky, A., Bamber, J.L., Chassignet, E., Hu, X., Lee, C.M., Somavilla, R., 2016. Greenland freshwater pathways in the sub-Arctic Seas from model experiments with passive tracers. *J. Geophys. Res.: Oceans* 121 (1), 877–907. <http://dx.doi.org/10.1002/2015JC011290>.
- Eden, C., Böning, C., 2002. Sources of eddy kinetic energy in the labrador sea. *J. Phys. Oceanogr.* 32 (12), 3346–3363. [http://dx.doi.org/10.1175/1520-0485\(2002\)032<3346:soekei>2.0.co;2](http://dx.doi.org/10.1175/1520-0485(2002)032<3346:soekei>2.0.co;2).
- Fox-Kemper, B., Ferrari, R., Hallberg, R., 2008. Parameterization of mixed layer eddies. Part I: Theory and diagnosis. *J. Phys. Oceanogr.* 38 (6), 1145–1165. <http://dx.doi.org/10.1175/2007JPO3792.1>.

- Fox-Kemper, B., Ferrari, R., Pedlosky, J., 2003. On the indeterminacy of rotational and divergent eddy fluxes. *J. Phys. Oceanogr.* 33 (2), 478–483. [http://dx.doi.org/10.1175/1520-0485\(2003\)033<0478:OTIORA>2.0.CO;2](http://dx.doi.org/10.1175/1520-0485(2003)033<0478:OTIORA>2.0.CO;2).
- Fröb, F., Olsen, A., Våge, K., Moore, G.W.K., Yashayaev, I., Jeansson, E., Rajasakaren, B., 2016. Irminger Sea deep convection injects oxygen and anthropogenic carbon to the ocean interior. *Nature Commun.* 7 (13244), <http://dx.doi.org/10.1038/ncomms13244>.
- Gaube, P., McGillicuddy, D.J., Moulin, A.J., 2019. Mesoscale eddies modulate mixed layer depth globally. *Geophys. Res. Lett.* 46 (3), 1505–1512. <http://dx.doi.org/10.1029/2018gl080006>.
- Gelderloos, R., Katsman, C.A., Drijfhout, S.S., 2011. Assessing the roles of three eddy types in restratifying the Labrador Sea after deep convection. *J. Phys. Oceanogr.* 41 (11), 2102–2119. <http://dx.doi.org/10.1175/JPO-D-11-054.1>.
- Gent, P.R., McWilliams, J.C., 1990. Isopycnal mixing in ocean circulation models. *J. Phys. Oceanogr.* 20 (1), 150–155. [http://dx.doi.org/10.1175/1520-0485\(1990\)020<0150:IMIOCM>2.0.CO;2](http://dx.doi.org/10.1175/1520-0485(1990)020<0150:IMIOCM>2.0.CO;2).
- Gillard, L.C., Pennelly, C., Johnson, H.L., Myers, P.G., 2022. The effects of atmospheric and lateral buoyancy fluxes on Labrador sea mixed layer depth. *Ocean Model.* 171, 101974. <http://dx.doi.org/10.1016/j.ocemod.2022.101974>.
- Good, S.A., Martin, M.J., Rayner, N.A., 2013. EN4: Quality controlled ocean temperature and salinity profiles and monthly objective analyses with uncertainty estimates. *J. Geophys. Res.: Oceans* 118 (12), 6704–6716. <http://dx.doi.org/10.1002/2013jc009067>.
- Griffies, S.M., Danabasoglu, G., Durack, P.J., Adcroft, A.J., Balaji, V., Böning, C.W., Chassignet, E.P., Curchitser, E., Deshayes, J., Drange, H., Fox-Kemper, B., Gleckler, P.J., Gregory, J.M., Haak, H., Hallberg, R.W., Heimbach, P., Hewitt, H.T., Holland, D.M., Ilyina, T., JungCLAUS, J.H., Komuro, Y., Krasting, J.P., Large, W.G., Marsland, S.J., Masina, S., McDougall, T.J., Nurser, A.J.G., Orr, J.C., Pirani, A., Qiao, F., Stouffer, R.J., Taylor, K.E., Treguier, A.M., Tsujino, H., Uotila, P., Valdivieso, M., Wang, Q., Winton, M., Yeager, S.G., 2016. OMIP contribution to CMIP6: experimental and diagnostic protocol for the physical component of the Ocean Model Intercomparison Project. *Geosci. Model Dev.* 9 (9), 3231–3296. <http://dx.doi.org/10.5194/gmd-9-3231-2016>.
- Griffies, S.M., Gnanadesikan, A., Pacanowski, R.C., Larichev, V.D., Dukowicz, J.K., Smith, R.D., 1998. Isonutral diffusion in a z-coordinate ocean model. *J. Phys. Oceanogr.* 28 (5), 805–830. [http://dx.doi.org/10.1175/1520-0485\(1998\)028<0805:IDIAZC>2.0.CO;2](http://dx.doi.org/10.1175/1520-0485(1998)028<0805:IDIAZC>2.0.CO;2).
- Griffies, S.M., Winton, M., Anderson, W.G., Benson, R., Delworth, T.L., Dufour, C.O., Dunne, J.P., Goddard, P., Morrison, A.K., Rosati, A., Wittenberg, A.T., Yin, J., Zhang, R., 2015. Impacts on ocean heat from transient mesoscale eddies in a hierarchy of climate models. *J. Clim.* 28 (3), 952–977. <http://dx.doi.org/10.1175/JCLI-D-14-00353.1>.
- Griffies, S.M., Winton, M., Samuels, B., Danabasoglu, G., Yeager, S.G., Marsland, S.J., Drange, H., Bentsen, M., 2012. Datasets and Protocol for the CLIVAR WGOMD Coordinated Ocean-Sea Ice Reference Experiments (CORES). WCRP Report No. 21/2012.
- Heuzé, C., 2021. Antarctic bottom water and north atlantic deep water in CMIP6 models. *Ocean Sci.* 17 (1), 59–90. <http://dx.doi.org/10.5194/os-17-59-2021>.
- Hu, S., Sprintall, J., Guan, C., McPhaden, M.J., Wang, F., Hu, D., Cai, W., 2020. Deep-reaching acceleration of global mean ocean circulation over the past two decades. *Sci. Adv.* 6 (6), <http://dx.doi.org/10.1126/sciadv.aax7727>.
- Hurrell, 2003. NAO Index Data Provided by the Climate Analysis Section. NCAR, Boulder, USA, updated regularly. Accessed 22 2021 at <https://climatedataguide.ucar.edu/climate-data/hurrell-north-atlantic-oscillation-nao-index-pc-based>.
- IOC, SCOR, IAPSO, 2010. The International Thermodynamic Equation of Seawater – 2010: Calculation and Use of Thermodynamic Properties. In: Intergovernmental Oceanographic Commission, Manuals and Guides, vol. 56, UNESCO.
- Jackett, D.R., McDougall, T.J., 1995. Minimal adjustment of hydrographic profiles to achieve static stability. *J. Atmos. Ocean. Technol.* 12 (2), 381–389. [http://dx.doi.org/10.1175/1520-0426\(1995\)012<0381:maohpt>2.0.co;2](http://dx.doi.org/10.1175/1520-0426(1995)012<0381:maohpt>2.0.co;2).
- Jayne, S.R., Marotzke, J., 2002. The oceanic eddy heat transport. *J. Phys. Oceanogr.* 32 (12), 3328–3345. [http://dx.doi.org/10.1175/1520-0485\(2002\)032<3328:TOEHT>2.0.CO;2](http://dx.doi.org/10.1175/1520-0485(2002)032<3328:TOEHT>2.0.CO;2).
- Jones, H., Marshall, J., 1997. Restratification after deep convection. *J. Phys. Oceanogr.* 27 (10), 2276–2287. [http://dx.doi.org/10.1175/1520-0485\(1997\)027<2276:RADC>2.0.CO;2](http://dx.doi.org/10.1175/1520-0485(1997)027<2276:RADC>2.0.CO;2).
- Kawasaki, T., Hasumi, H., 2014. Effect of freshwater from the West Greenland Current on the winter deep convection in the Labrador Sea. *Ocean Model.* 75, 51–64. <http://dx.doi.org/10.1016/j.ocemod.2014.01.003>.
- Kelley, D., Richards, C., 2022. oce: Analysis of oceanographic data. r package version 1.5-0 (2022). <https://CRAN.R-project.org/package=oce>.
- Koenig, T., Fuentes-Franco, R., Meccia, V.L., Gutjahr, O., Jackson, L.C., New, A.L., Ortega, P., Roberts, C.D., Roberts, M.J., Arsouze, T., Iovino, D., Moine, M.-P., Sein, D.V., 2021. Deep mixed ocean volume in the Labrador sea in HighResMIP models. *Clim. Dynam.* 57 (7–8), 1895–1918. <http://dx.doi.org/10.1007/s00382-021-05785-x>.
- Large, W.G., McWilliams, J.C., Doney, S.C., 1994. Oceanic vertical mixing: A review and a model with a nonlocal boundary layer parameterization. *Rev. Geophys.* 32 (4), 363–403. <http://dx.doi.org/10.1029/94RG01872>.
- Large, W.G., Yeager, S.G., 2009. The global climatology of an interannually varying air–sea flux data set. *J. Clim.* 33 (341), <http://dx.doi.org/10.1007/s00382-008-0441-3>.
- Lavender, K.L., Davis, R.E., Owens, W.B., 2002. Observations of open-ocean deep convection in the Labrador Sea from subsurface floats. *J. Phys. Oceanogr.* 32 (2), 511–526. [http://dx.doi.org/10.1175/1520-0485\(2002\)032<0511:OOODC>2.0.CO;2](http://dx.doi.org/10.1175/1520-0485(2002)032<0511:OOODC>2.0.CO;2).
- Lilly, J.M., Rhines, P.B., Schott, F., Lavender, K., Lazier, J.R.N., Send, U., 2003. Observations of the Labrador Sea Eddy Field. *Process Oceanogr.* 59 (1), 75–176.
- Locarnini, R.A., Mishonov, A.V., Antonov, J.I., Boyer, T.P., Garcia, H.E., Baranova, O.K., Zweng, M.M., Paver, C.R., Reagan, J.R., Johnson, D.R., Hamilton, M., Seidov, D., 2013. World Ocean Atlas 2013, Volume 1: Temperature. A Mishonov technical editor, NOAA Atlas NESDIS 73.
- Lorenz, E.N., 1955. Available potential energy and the maintenance of the general circulation. *Tellus* 7 (2), 157–167. <http://dx.doi.org/10.1111/j.2153-3490.1955.tb01148.x>.
- Luo, H., Bracco, A., Yashayaev, I., Lorenzo, E.D., 2012. The interannual variability of potential temperature in the central Labrador sea. *J. Geophys. Res.: Oceans* 117 (C10), <http://dx.doi.org/10.1029/2012jc007988>.
- Marchesiello, P., McWilliams, J.C., Shchepetkin, A., 2003. Equilibrium structure and dynamics of the California Current system. *J. Phys. Oceanogr.* 33 (4), 753–783. [http://dx.doi.org/10.1175/1520-0485\(2003\)33<753:ESADOT>2.0.CO;2](http://dx.doi.org/10.1175/1520-0485(2003)33<753:ESADOT>2.0.CO;2).
- Marshall, J., Schott, F., 1999. Open-ocean convection: Observations, theory, and models. *Rev. Geophys.* 37 (1), 1–64.
- Marshall, J., Shutts, G., 1981. A note on rotational and divergent eddy fluxes. *J. Phys. Oceanogr.* 11 (12), 1677–1680. [http://dx.doi.org/10.1175/1520-0485\(1981\)011<1677:ANORAD>2.0.CO;2](http://dx.doi.org/10.1175/1520-0485(1981)011<1677:ANORAD>2.0.CO;2).
- Martínez-Moreno, J., Hogg, A.M., England, M.H., Constantinou, N.C., Kiss, A.E., Morrison, A.K., 2021. Global changes in oceanic mesoscale currents over the satellite altimetry record. *Nature Clim. Change* 11 (5), 397–403. <http://dx.doi.org/10.1038/s41558-021-01006-9>.
- McGeehan, T., Maslowski, W., 2011. Impact of shelf–basin freshwater transport on deep convection in the Western Labrador Sea. *J. Phys. Oceanogr.* 41 (11), 2187–2210. <http://dx.doi.org/10.1175/JPO-D-11-01.1>.
- Morrison, A.K., Saenko, O.A., Hogg, A.M., Spence, P., 2013. The role of vertical eddy flux in southern ocean heat uptake. *Geophys. Res. Lett.* 40 (20), 5445–5450. <http://dx.doi.org/10.1002/2013gl057706>.
- Olbers, D., Willebrand, J., Eden, C., 2012. *Ocean Dynamics*. Springer, Berlin, Heidelberg, <http://dx.doi.org/10.1007/978-3-642-23450-7>.
- Pacini, A., Pickart, R.S., 2022. Meanders of the west greenland current near cape farewell. *Deep Sea Res. Part I: Oceanographic Res. Pap.* 179, 103664. <http://dx.doi.org/10.1016/j.dsr.2021.103664>.
- Palter, J.B., Lozier, M.S., Lavender, K.L., 2008. How does Labrador Sea water enter the deep western boundary current? *J. Phys. Oceanogr.* 38 (5), 968–983. <http://dx.doi.org/10.1175/2007JPO3807.1>.
- Pebesma, E., 2018. Simple features for R: Standardized support for spatial vector data. *R. J.* 10 (1), 439–446. <http://dx.doi.org/10.32614/RJ-2018-009>.
- Pennelly, C., Myers, P.G., 2022. Tracking irmlinger rings' properties using a sub-mesoscale ocean model. *Prog. Oceanogr.* 201, 102735. <http://dx.doi.org/10.1016/j.pocean.2021.102735>, <https://www.sciencedirect.com/science/article/pii/S0079661121002184>.
- Redi, M.H., 1982. Oceanic isopycnal mixing by coordinate rotation. *J. Phys. Oceanogr.* 12 (10), 1154–1158. [http://dx.doi.org/10.1175/1520-0485\(1982\)012<1154:OIMBCR>2.0.CO;2](http://dx.doi.org/10.1175/1520-0485(1982)012<1154:OIMBCR>2.0.CO;2).
- Renault, L., Molemaker, M.J., McWilliams, J.C., Shchepetkin, A.F., Lemarié, F., Chelton, D., Illig, S., Hall, A., 2016. Modulation of wind work by oceanic current interaction with the atmosphere. *J. Phys. Oceanogr.* 46 (6), 1685–1704. <http://dx.doi.org/10.1175/JPO-D-15-0232.1>.
- Rhein, M., Steinfeldt, R., Kieke, D., Stendardo, I., Yashayaev, I., 2017. Ventilation variability of Labrador sea water and its impact on oxygen and anthropogenic carbon: a review. *Phil. Trans. R. Soc. A* 375 (2102), 20160321. <http://dx.doi.org/10.1098/rsta.2016.0321>.
- Rieck, J.K., Böning, C.W., Getzlaff, K., 2019. The nature of eddy kinetic energy in the Labrador Sea: Different types of mesoscale eddies, their temporal variability, and impact on deep convection. *J. Phys. Oceanogr.* 49 (8), 2075–2094. <http://dx.doi.org/10.1175/JPO-D-18-0243.1>.
- Rieck, J.K., Böning, C.W., Greatbatch, R.J., Scheinert, M., 2015. Seasonal variability of eddy kinetic energy in a global high-resolution ocean model. *Geophys. Res. Lett.* 42 (21), 9379–9386. <http://dx.doi.org/10.1002/2015gl066152>.
- Rimac, A., von Storch, J.-S., Eden, C., 2016. The total energy flux leaving the ocean's mixed layer. *J. Phys. Oceanogr.* 46 (6), 1885–1900. <http://dx.doi.org/10.1175/jpo-d-15-0115.1>.
- Röske, F., 2006. A global heat and freshwater forcing dataset for ocean models. *Ocean Model.* 11 (3–4), 235–297. <http://dx.doi.org/10.1016/j.ocemod.2004.12.005>.
- Rykova, T., Straneo, F., Bower, A.S., 2015. Seasonal and interannual variability of the West Greenland Current System in the Labrador Sea in 1993–2008. *J. Geophys. Res.: Oceans* 120 (2), 1318–1332. <http://dx.doi.org/10.1002/2014JC010386>.
- Rykova, T., Straneo, F., Lilly, J.M., Yashayaev, I., 2009. Irminger Current Anticyclones in the Labrador Sea observed in the hydrographic record, 1990–2004. *J. Mar. Res.* 67 (3), 361–384. <http://dx.doi.org/10.1357/002224009789954739>.

- Saenko, O.A., 2015. Strong eddy compensation for the gulf stream heat transport. *Geophys. Research Lett.* 42 (24), <http://dx.doi.org/10.1002/2015gl066111>.
- Saenko, O.A., Dupont, F., Yang, D., Myers, P.G., Yashayaev, I., Smith, G.C., 2014. Role of resolved and parameterized eddies in the Labrador Sea balance of heat and buoyancy. *J. Phys. Oceanogr.* 44 (12), 3008–3032. <http://dx.doi.org/10.1175/JPO-D-14-0041.1>.
- Schmidt, S., Send, U., 2007. Origin and composition of seasonal Labrador Sea freshwater. *J. Phys. Oceanogr.* 37 (6), 1445–1454. <http://dx.doi.org/10.1175/jpo3065.1>.
- Scholz, P., Kieke, D., Lohmann, G., Ionita, M., Rhein, M., 2014. Evaluation of Labrador Sea Water formation in a global Finite-Element Sea-Ice Ocean Model setup, based on a comparison with observational data. *J. Geophys. Res.: Oceans* 119 (3), 1644–1667. <http://dx.doi.org/10.1002/2013JC009232>.
- Steele, M., Morley, R., Ermold, W., 2001. PHC: A global ocean hydrography with a high-quality Arctic Ocean. *J. Clim.* 14 (9), 2079–2087. [http://dx.doi.org/10.1175/1520-0442\(2001\)014<2079:PAGOHW>2.0.CO;2](http://dx.doi.org/10.1175/1520-0442(2001)014<2079:PAGOHW>2.0.CO;2).
- von Storch, J.-S., Sasaki, H., Marotzke, J., 2007. Wind-generated power input to the deep ocean: An estimate using a $1/10^\circ$ general circulation model. *J. Phys. Oceanogr.* 37 (3), 657–672. <http://dx.doi.org/10.1175/jpo3001.1>.
- Straneo, F., 2006. Heat and Freshwater Transport through the Central Labrador Sea. *J. Phys. Oceanogr.* 36 (4), 606–628.
- Tagklis, F., Bracco, A., Ito, T., Castelao, R.M., 2020. Submesoscale modulation of deep water formation in the Labrador sea. *Sci. Rep.* 10 (1), <http://dx.doi.org/10.1038/s41598-020-74345-w>.
- Thomas, M.D., Zhang, R., 2022. Two sources of deep decadal variability in the central Labrador sea open-ocean convection region. *Geophys. Res. Lett.* 49 (11), e2022GL098825, e2022GL098825 2022GL098825. <http://dx.doi.org/10.1029/2022GL098825>, arXiv:<https://agupubs.onlinelibrary.wiley.com/doi/pdf/10.1029/2022GL098825>, <https://agupubs.onlinelibrary.wiley.com/doi/abs/10.1029/2022GL098825>.
- Vallis, G.K., 2017. *Atmospheric and Oceanic Fluid Dynamics – Fundamentals and Large-Scale Circulation*, second ed. Cambridge University Press.
- von Storch, J.-S., Eden, C., Fast, I., Haak, H., Hernández-Deckers, D., Maier-Reimer, E., Marotzke, J., Stammer, D., 2012. An estimate of the Lorenz energy cycle for the world ocean based on the STORM/NCEP simulation. *J. Phys. Oceanogr.* 42 (12), 2185–2205. <http://dx.doi.org/10.1175/JPO-D-12-079.1>.
- Wang, Q., Danilov, S., Sidorenko, D., Timmermann, R., Wekerle, C., Wang, X., Jung, T., Schröter, J., 2014. The Finite Element Sea Ice-Ocean Model (FESOM) v1.4: formulation of an ocean general circulation model. *Geosci. Model Dev.* 7 (2), 663–693. <http://dx.doi.org/10.5194/gmd-7-663-2014>.
- Wekerle, C., Wang, Q., von Appen, W.-J., Danilov, S., Schourup-Kristensen, V., Jung, T., 2017. Eddy-resolving simulation of the Atlantic water circulation in the Fram Strait with focus on the seasonal cycle. *J. Geophys. Res.: Oceans* 122 (11), 8385–8405. <http://dx.doi.org/10.1002/2017JC012974>.
- Yashayaev, I., Loder, J.W., 2016. Recurrent replenishment of Labrador Sea Water and associated decadal-scale variability. *J. Geophys. Res.: Oceans* 121 (11), 8095–8114. <http://dx.doi.org/10.1002/2016JC012046>.
- Yeager, S., Castruccio, F., Chang, P., Danabasoglu, G., Maroon, E., Small, J., Wang, H., Wu, L., Zhang, S., 2021. An outsized role for the Labrador sea in the multidecadal variability of the Atlantic overturning circulation. *Sci. Adv.* 7 (41), <http://dx.doi.org/10.1126/sciadv.abb3592>.
- Zdunkowski, W., Bott, A., 2003. *The Helmholtz Theorem*. Cambridge University Press, pp. 214–217. <http://dx.doi.org/10.1017/CBO9780511805462.014>.
- Zhang, Z., Wang, W., Qiu, B., 2014. Oceanic mass transport by mesoscale eddies. *Science* 345 (6194), 322–324. <http://dx.doi.org/10.1126/science.1252418>.
- Zhang, W., Yan, X.-H., 2014. Lateral heat exchange after the Labrador Sea deep convection in 2008. *J. Phys. Oceanogr.* 44 (12), 2991–3007. <http://dx.doi.org/10.1175/JPO-D-13-0198.1>.
- Zhang, W., Yan, X.-H., 2018. Variability of the Labrador Sea surface eddy kinetic energy observed by altimeter from 1993 to 2012. *J. Geophys. Res.: Oceans* 123 (1), 601–612. <http://dx.doi.org/10.1002/2017JC013508>.
- Zou, S., Bower, A.S., Furey, H., Pickart, R.S., Houpert, L., Holliday, N.P., 2021. Observed deep cyclonic eddies around southern Greenland. *J. Phys. Oceanogr.* <http://dx.doi.org/10.1175/jpo-d-20-0288.1>.